Overview of the Alcator C-MOD research programme

S. Scott[1], A. Bader[2], M. Bakhtiari[3], N. Basse[2,a] W. Beck[2], T. Biewer[4],
S. Bernabei[1], P. Bonoli[2], B. Bose[2], R. Bravenec[5], I. Bespamyatnov[5], R. Childs[2],
I. Cziegler[2], R. Doerner[6], E. Edlund[2], D. Ernst[2], A. Fasoli[7], M. Ferrara[2],
C. Fiore[2], T. Fredian[2], A. Graf[8], T. Graves[2], R. Granetz[2], N. Greenough[1],
M. Greenwald[2], M. Grimes[2], O. Grulke[9], D. Gwinn[10], R. Harvey[11], S. Harrison[3],
T. C. Hender[12], J. Hosea[1], D. F. Howell[12], A. E. Hubbard[2], J. W. Hughes[2],
I. Hutchinson[2], A. Ince-Cushman[2], J. Irby[2], T. Jernigan[4], D. Johnson[2], J. Ko[2],
P. Koert[2], B. LaBombard[2], A. Kanojia[2], L. Lin[2], Y. Lin[2], B. Lipschultz[2],
J. Liptac[2,b], A. Lynn[14,c], P. MacGibbon[2], E. Marmar[2], K. Marr[2], M. May[13],
D. R. Mikkelsen[1], R. McDermott[2], A. Parisot[2], R. Parker[2], C. K. Phillips[1],
P. Phillips[5], M. Porkolab[2], M. Reinke[2], J. Rice[2], W. Rowan[5], M. Sampsell[5],
G. Schilling[1], A. Schmidt[2], N. Smick[2], A. Smirnov[11], J. Snipes[2], D. Stotler[1],
J. Stillerman[2], V. Tang[13,d], D. Terry[2], J. Terry[2], M. Ulrickson[14], R. Vieira[2],
G. Wallace[2], D. Whyte[2], J. R. Wilson[1], G. Wright[3], J. Wright[2], S. Wolfe[2],
S. Wukitch[2], G. Wurden[15], H. Yuh[16], K. Zhurovich[2], J. Zaks[2] and S. Zweben[1]

[1] Princeton Plasma Physics Laboratory, Princeton University, PO Box 451, Princeton, NJ 08543, USA
[2] Massachusetts Institute of Technology, Plasma Science and Fusion Center, 175 Albany Street, Cambridge, MA 02139, USA
[3] University of Wisconsin, 1500 Engineering Drive, Madison, WI 53706, USA
[4] Oak Ridge National Laboratory, Fusion Energy Division, PO Box 2008, Oak Ridge, TN 37831, USA
[5] University of Texas at Austin, 1 University Station, C1510, Austin, TX 78712, USA
[6] University of California, San Diego, La Jolla, CA 92093, USA
[7] Centre de Recherches en Physique des Plasmas Association EURATOM - Confédération Suisse Ecole Polytechnique Fédérale, Station 13 CH-1015 Lausanne, Switzerland
[8] Department of Physics, University of California, One Shields Avenue, Davis, CA 95616, USA
[9] Max-Planck-Institut für Plasmaphysik, Teilinstitut Greifswald, Wendelsteinstraße 1, D-17491 Greifswald, Germany
[10] Bagley Associates, 7 Bagley Avenue, Lowell, MA 01851, USA
[11] CompX, PO Box 2672, Del Mar, CA 92014, USA
[12] EURATOM-UKAEA Fusion Association, Culham Science Centre, Abingdon, OX14 3DB, UK
[13] Lawrence Livermore National Laboratory, 7000 East Avenue, Livermore, CA 99550, USA
[14] Fusion Energy Science Program, Sandia National Laboratories, PO Box 5800, MS-1129, Albuquerque, NM 87185, USA
[15] Los Alamos National Laboratory, PO Box 1663, Los Alamos, NM 87545, USA
[16] Nova Photonics, Inc., One Oak Place, Princeton, NJ 08540, USA

E-mail: sscott@pppl.gov

Abstract
Alcator C-MOD has compared plasma performance with plasma-facing components (PFCs) coated with boron to all-metal PFCs to assess projections of energy confinement from current experiments to next-generation burning

[a] Current address: ABB Switzerland Ltd, Corporate Research, Segelhof-strasse 1 K, CH-5405 Baden 5 Dättwil, Switzerland.
[b] Current address: Intel Corporation, Hillsboro, OR, USA.
[c] Current address: Department of Electrical and Computer Engineering, MSCO1 1100, University of New Mexico, NM 87131, USA.
[d] Current address: Lawrence Livermore National Laboratory, PO Box 808, L-229, Livermore, CA 94551, USA.

tokamak plasmas. Low-Z coatings reduce metallic impurity influx and diminish radiative losses leading to higher H-mode pedestal pressure that improves global energy confinement through profile stiffness. RF sheath rectification along flux tubes that intersect the RF antenna is found to be a major cause of localized boron erosion and impurity generation. Initial lower hybrid current drive (LHCD) experiments ($P_{LH} < 900\,kW$) in preparation for future advanced-tokamak studies have demonstrated fully non-inductive current drive at $I_p \sim 1.0\,MA$ with good efficiency, $I_{drive} = 0.4 P_{LH}/n_{eo}R$ (MA, MW, $10^{20}\,m^{-3}$,m). The potential to mitigate disruptions in ITER through massive gas-jet impurity puffing has been extended to significantly higher plasma pressures and shorter disruption times. The fraction of total plasma energy radiated increases with the Z of the impurity gas, reaching 90% for krypton. A positive major-radius scaling of the error field threshold for locked modes ($B_{th}/B \propto R^{0.68\pm0.19}$) is inferred from its measured variation with B_T that implies a favourable threshold value for ITER. A phase contrast imaging diagnostic has been used to study the structure of Alfvén cascades and turbulent density fluctuations in plasmas with an internal transport barrier. Understanding the mechanisms responsible for regulating the H-mode pedestal height is also crucial for projecting performance in ITER. Modelling of H-mode edge fuelling indicates high self-screening to neutrals in the pedestal and scrape-off layer (SOL), and reproduces experimental density pedestal response to changes in neutral source, including a weak variation of pedestal height and constant width. Pressure gradients in the near SOL of Ohmic L-mode plasmas are observed to scale consistently as I_p^2, and show a significant dependence on X-point topology. Fast camera images of intermittent turbulent structures at the plasma edge show they travel coherently through the SOL with a broad radial velocity distribution having a peak at about 1% of the ion sound speed, in qualitative agreement with theoretical models. Fast D_α diagnostics during gas puff imaging show a complex behaviour of discrete ELMs, starting with an $n \approx 10$ precursor oscillation followed by a rapid primary ejection as the pedestal crashes and then multiple, slower secondary ejections.

PACS numbers: 52.25.Vy, 52.35.Bj, 52.35.Ra, 52.40.Hf, 52.55.−s, 52.55.Fa, 52.55.Wq

1. Introduction

Recent research on the high-field, high-density diverted Alcator C-MOD tokamak has focused on the plasma physics and plasma engineering required for ITER and for attractive fusion reactors. C-MOD is prototypical of ITER in several key respects including toroidal magnetic field, equilibrated ions and electrons, plasma density, power density in the scrape-off-layer (SOL), low momentum input, high-Z plasma-facing components (PFCs), divertor neutral opacity and long-pulse length compared with the skin time. The paper is organized as follows: sections 2 and 3 summarize the major thrusts of the C-MOD 2005-6 campaigns comprising performance studies with all-metal walls and initial lower hybrid current drive (LHCD) experiments. Recent disruption mitigation studies involving massive gas puffs are described in section 4. Experiments to infer the major-radius scaling of the error field threshold for locked modes are reported in section 5. Sections 6 and 7 describe new results from the phase contrast imaging (PCI) diagnostic related to the stucture of Alfvén Cascades and the wavenumber spectrum of trapped electron mode (TEM) turbulence. The next four sections cover recent progress in the physics of the edge plasma. New studies of the scaling of pressure gradients in the H-mode pedestal and SOL are summarized in sections 8 and 9. Sections 10 and 11 report new results in imaging turbulence in the edge plasma and measurements of the dynamics of edge localized modes. Planned facility upgrades to C-MOD over the next two years are described in section 12.

2. Performance with all-metal walls versus low-Z coatings

Tungsten has been selected as the primary material for PFCs in ITER and fusion reactors based on its low tritium retention, low erosion rate, and low neutron damage rate. High-Z metallic PFCs including molybdenum and tungsten have hydrogen recycling and radiative properties that differ substantially from low-Z PFCs (carbon, beryllium) and low-Z PFCs coatings (boron, beryllium, lithium). Most of the world's divertor and confinement database has been developed in tokamaks with low-Z PFCs or low-Z PFCs coatings (with ASDEX [1] currently pursuing an all-tungsten PFCs environment), but carbon has been relegated to a small fraction of the PFCs surfaces in ITER and none in a high-fluence demonstration reactor due to concerns related to tritium retention and erosion.

Until recently, the PFCs environment in C-MOD has been molybdenum coated with a thin layer of boron, plus boron-nitride protective tiles near the RF antennas. In C-MOD, the boron layer is replenished periodically using a low-temperature electron cyclotron plasma discharge fuelled with diborane gas. This 'boronization' process is typically carried out overnight, depositing about 200 nm of boron over a period of 10–12 h, and the resonance location can be swept from the inner wall to beyond the outer limiters by scanning the toroidal field. The deposition location can also be localized radially by imposing a small variation in toroidal field. Prior to the 2005 experimental campaign, boron was removed from all PFCs and the boron-nitride tiles were replaced with molybdenum tiles to allow a direct comparison of plasma performance with and without a boron coating, yielding a surface concentration
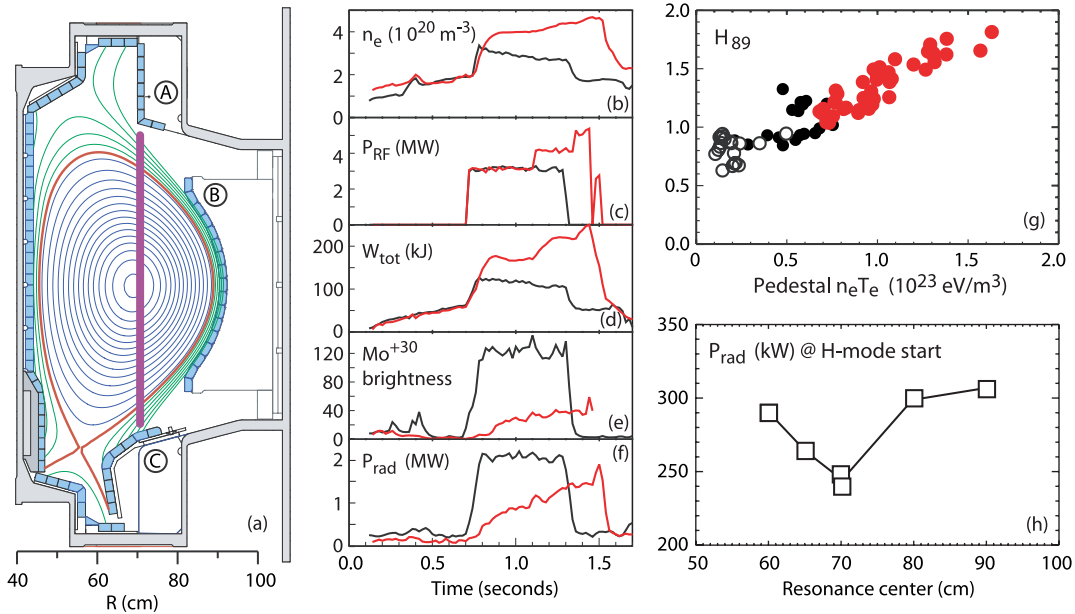
Figure 1. (*a*) Optimized boronization resonance deposits boron onto upper gusset tiles (A) and lower outer divertor (C) . (*b*)–(*f*) Comparison of plasma performance with (red) and without boron (black) coating. (*g*) Energy confinement parameter H_{89P} as a function of pedestal pressure with (red) and without (black) boron coating. Open symbols represent L-mode and solid symbols represent H-mode plasmas. (*h*) Radiated power shortly after L–H transition as a function of boron deposition, showing optimum location at $R \approx 70$ cm.

of 80–90% Mo with 10–20% residual B. H-mode plasmas were readily obtained during RF heating with pure Mo (i.e. uncoated) PFCs, but the impurity concentration was high ($n_{Mo}/n_e \leqslant 0.1\%$), radiated power was high, and energy confinement was degraded, with $\tau_E = 0.9 - 1.3 \times \tau_{E89P}$ [2]. This was due to local cooling of the pedestal by Mo radiation (the dominant radiator in C-MOD) which lowers the pedestal pressure and propagates to lower plasma core pressures and global stored energy through profile stiffness (figure 1(*g*)). After applying boron coatings n_{Mo}/n_e was reduced by a factor of 10–20 with H_{89P} approaching 2. The boronized discharge illustrated in figures 1(*b*)–(*f*) obtained a world-record volume averaged plasma pressure ($\langle p \rangle = 1.8$ atm) at $\beta_n = 1.74$. The beneficial effects of overnight boronization last 20–50 high-power discharges, with radiated power rising monotonically shot-to-shot and with reduced τ_E visible after about 50 MJ of total deposited energy in ICRF-heated discharges.

A body of evidence suggests that the boron erosion is spatially localized: prior to the 2005 campaign vessel cleaning, boron layers averaging 6000 nm thick were measured on a poloidal array of tiles, indicating that the majority of PFCs surfaces experienced little boron erosion. By contrast, the outer divertor surfaces extending from the bottom of the outer divertor vertical section to $R \approx 0.67$ m showed the highest Mo surface concentrations (10–50%), presumably due to net erosion of the boron layers by the high particle and heat fluxes to those surfaces. Brief, between-discharge boronization (BDB) has been utilized as a diagnostic of the erosion location. A thin (10 nm) boron layer was applied locally in major radius as the resonance was swept ± 5 cm. The layer eroded in just 1–2 shots, allowing controlled studies of the boron effectiveness. Figure 1(*h*) illustrates that there is a pronounced optimum location for boron deposition at $R \approx 70$ cm, suggesting that replenishing the boron layer at the top of the outer divertor and

the upper gusset tiles (location A in figure 1) is particularly important (figure 3(*a*)).

RF sheath rectification. Recent experiments suggest that both boron erosion and Mo impurity generation in Alcator C-MOD are strongly affected by RF sheath-rectification [3, 4] along flux tubes that intersect with or pass in front of the RF antenna [5]. Impurity generation driven by rectified RF sheaths is commonly observed in other tokamaks, including Textor [6], Tore Supra [7], TFTR [8] and JET [9]. In Alcator C-MOD, the flux tubes intersect the upper part of the outer limiters, upper gusset tiles and the top of the outer divertor, precisely where little boron accumulation was observed. Controlled studies with BDB show that RF-heated plasmas suffer increased radiation after just a single shot while Ohmic H-mode plasmas with comparable total energy input experience increased radiation only after 4–6 shots, suggesting that RF waves themselves rather than just total energy/particle fluence to the PFCs are important in the erosion mechanism. This conjecture was convincingly demonstrated by depositing a thin layer of boron with BDB followed by a series of RF-heated plasma discharges without further boron deposition. Performance degradation was observed on the second discharge if the same RF antenna was used but not if a different RF antenna was used on the second shot, proving that each antenna is associated with a different erosion location.

Deuterium retention. Following ultrasonic cleaning of PFCs tiles, deuterium retention was measured in a series of six Ohmic, non-disruptive plasmas in a predominantly high-Z PFCs environment. Low deuterium retention of order 0.1% was expected in Mo on the basis of previous measurements using ion beams incident on Mo target samples [10], but surprisingly the fraction of injected gas retained in the C-MOD
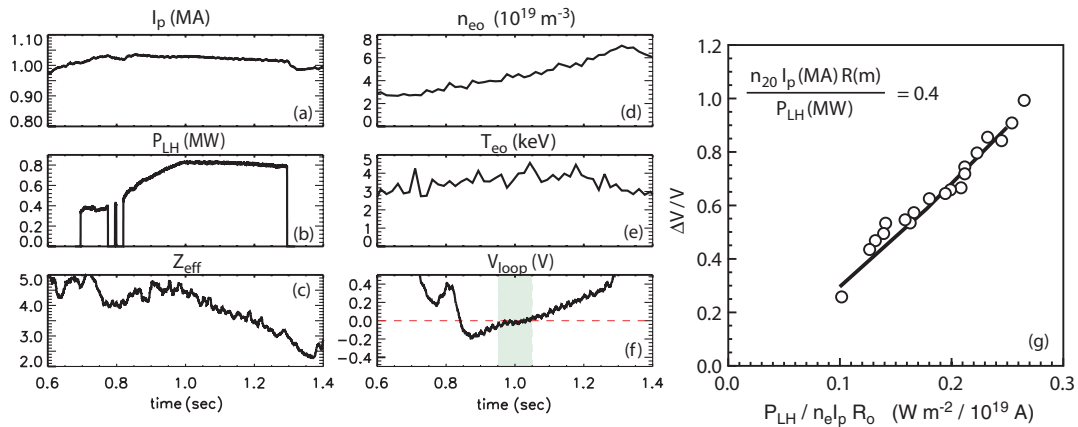
Figure 2. (*a*)–(*f*) Waveforms of conditions in discharge with ∼1 MA current driven by LHCD. Shaded green region represents ∼100 ms interval with near-zero loop voltage. (g) Analysis of current drive efficiency in a lower hybrid power scan at $n_\parallel = 1.6$, $P_{LH} = 120$–830 kW, $I_p = 0.7$–1.0 MA and $\bar{n}_e = (3.5$–$7.0) \times 10^{19}$ m^{-3}.

vessel surfaces was ∼45% in the first discharge, decreasing to a quasi-steady-state value of ∼30% by the end of the shot sequence. Similar retention values were observed on boronized PFCs. These retention rates are roughly comparable to those observed for tritium with carbon PFCs in TFTR [11] and JET [12] and represent a potential tritium-inventory issue for ITER [13].

Measurements of deuterium retention and depth profile during low-temperature plasma bombardment of a pure Mo target in the Dionisos facility [14] also indicate unexpectedly high levels of retained deuterium (∼0.25% of incident flux retained; surface atomic ratio D/Mo ∼ 1%) and deep deuterium penetration (⩾5000 nm). A candidate mechanism for apparent discrepancy between retention measurements with high-energy (∼5 keV) ion beams versus low energy, high-flux plasma is that the plasma generates *D* trapping sites at the surface that migrate into the bulk.

3. Lower-hybrid current drive

A major goal of the C-MOD program is achieving high performance advanced-tokamak (AT) plasmas with up to 1 MA non-inductive current (70% bootstrap, 30% LHCD) at high confinement ($H_{89P} \approx 2.5$) and high normalized beta ($\beta_n \leqslant 3$), and sustaining this performance for several current relaxation times. An objective of the lower hybrid programme is to provide information for the decision on installing LHCD capability on ITER and to support AT physics research. The C-MOD LHCD system comprises 12 klystron tubes with 3 MW total source power, a rear and front waveguide assembly, and a 4 × 24 plasma-facing waveguide coupler. It has the capability to vary the launched $n_\parallel$ spectrum over the range $n_\parallel = 1.5$–4.5 on a rapid time scale (∼1 ms), thereby potentially providing control of the radial location of driven current. The original coupler fabricated from a titanium alloy suffered serious and rapid erosion when exposed to C-MOD plasmas by an as-yet undetermined mechanism. In 2006 it was replaced by a stainless steel coupler which has functioned well, with no surface erosion and only minor melting observed on the edge waveguides after a full 14 week run campaign.

The first lower hybrid experimental campaign was limited to L-mode plasmas without ICRF heating at modest density. Initial results are quite encouraging: over 900 kW of power have been coupled to C-MOD plasmas with a coupling efficiency that is consistent with code predictions [15] when the density profile immediately in front of the LH grill is modelled by a small (∼1 mm) vacuum gap followed by a step-wise increase to a level consistent with probe measurements, then a further increase with a constant density gradient [16]. As shown in figure 2, 800 kW of coupled LH power drove the surface loop voltage negative or near zero for approximately 100 ms (≈ τ_{CR}) in a $I_p = 1.0$ MA plasma at $n_{eo} \approx 4 \times 10^{19}$ m^{-3}, consistent with current drive efficiency calculations by the GENRAY-CQl3D [17] model. The loop voltage increased later on in the discharge as the density rose to 7×10^{19} m^{-3} thereby decreasing the driven current below 1 MA. We have also observed sawtooth stabilization at $I_p = 700$ kW, $\bar{n}_e = 4.4 \times 10^{19}$ m^{-3} with $P_{LH} \approx 750$ kW that indicates significant off-axis current drive. The central electron temperature increased from 2.6 to 3.7 keV due to the combined effects of electron heating by the LH waves and cessation of the sawteeth. Overall, the energy confinement during LH heating appears to be consistent with that of low density Ohmic, and no unusual impurity influx is observed.

We applied the method developed by Giruzzi [18] to assess the current drive efficiency in plasmas for which the loop voltage does not go to zero. The fractional change in loop voltage, $\Delta V / V$ was measured in a lower hybrid power scan at fixed plasma density and current. The current drive efficiency inferred from this analysis (figure 2(*g*)) is at the upper end of the range expected theoretically, ($I_{drive} = 0.4 P_{LH}$ (MW) /n_{eo} (10^{20} m^{-3}) R (m)). The coefficient is 0.28 if $\bar{n}_e$ rather than n_{eo} is used as the density normalization.

4. Disruption mitigation

Disruption-induced damage arising from high-power loads on divertor surfaces, generation of large relativistic electron runaway currents, and electromagnetic loads on conducting structures due to halo currents are major concerns for ITER and tokamak reactors. The technique of disruption mitigation
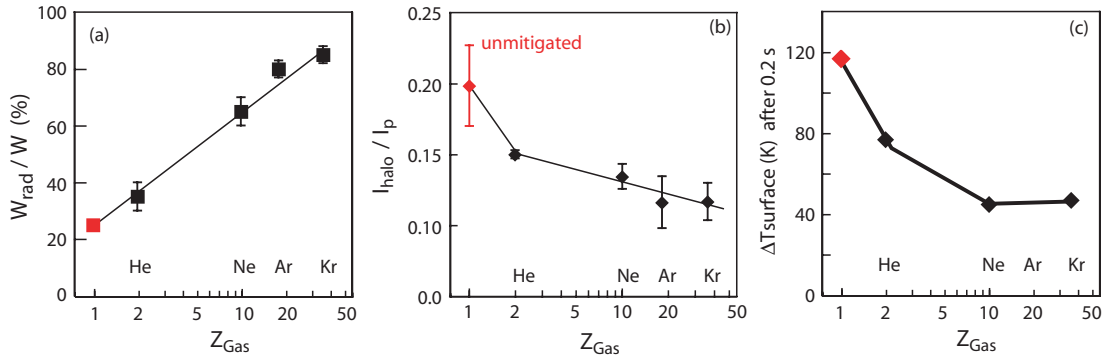
Figure 3. (*a*) Fraction of total power radiated during the disruption; (*b*) normalized halo current versus atomic number of mitigating gas; (*c*) rise in surface temperature at the outer lower divertor surface following disruption.

through massive gas-jet impurity puffing originally developed on DIII-D [19] has been extended to significantly higher plasma pressures and shorter disruption times. An ORNL fast-response valve delivered short, massive puffs of helium, neon, argon, or krypton gas to a delivery nozzle near the outer plasma edge. As shown in figure 3(*a*), the fraction of total plasma energy radiated increased with Z of the impurity gas, reaching 90% for krypton [20]. The increased radiated power cools the plasma during the current quench and additionally the impurity increases Z_{eff}, both of which decrease the L/R quench time. Consequently, the disruption-migrated plasma has less time to move vertically before contacting the torus wall, thereby reducing the disruption halo currents by up to ~50% (figure 3(*b*)). Infrared camera images of the outboard divertor tiles show less surface heating in migitated disruptions (figure 3(*c*)), consistent with the loss of most of the plasma energy to isotropic radiation. Studies of disruption mitigation with mixtures of helium and argon show promise in combining the favourable radiative properties of a high-Z gas with the rapid transit of helium through the gas delivery system, which is limited by its thermal speed.

High speed imaging of the gas-jet plumes show that impurity neutrals do not penetrate deeply into the plasma and initially cool just the periphery of the plasma. Nevertheless, within a few hundred microseconds some impurity ions appear in the plasma core and the core temperature decreases on the same time scale. NIMROD MHD simulations indicate that the initial edge cooling triggers rapid growth of 2/1 and 1/1 tearing modes resulting in a large stochastic region that mixes impurity ions into the core [21].

5. Scaling of the locked-mode threshold

A major uncertainty for projecting the error field threshold for locked modes on ITER is its scaling with major radius. The error field scaling is typically represented as a power law [22], $B_{err}/B_t \propto n^{\alpha_n} B^{\alpha_B} q^{\alpha_q} R^{\alpha_R}$. Dimensional scaling imposes the constraint $\alpha_R = 2\alpha_n + 1.25\alpha_B$ and experiments have established that $\alpha_n = 1$, thus a knowledge of the scaling with toroidal field (α_B) also determines the scaling with machine size. Unfortunately, scaling experiments in C-MOD, JET, DIII-D, and COMPASS-D have yielded disparate values of α_B [23, 24]. C-MOD executed a controlled toroidal field scan at fixed plasma shape (lower single null), fixed $q_{95} = 3.5$,
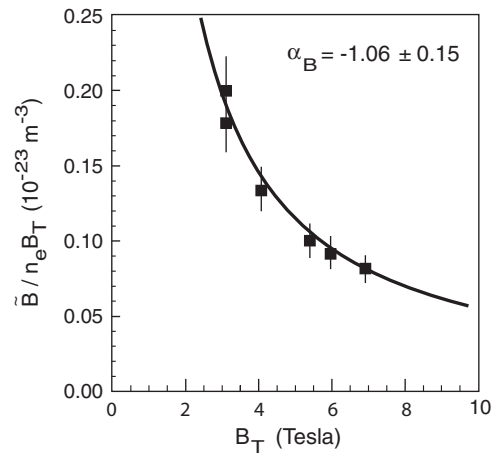

Figure 4. Scaling of error field required for mode-locking as a function of B_T.

$n/n_G = 0.18$. On each discharge, the error field imposed by external coils (predominantly $m/n = 1/1$, 2/1 with small 3/1 component) was ramped in magnitude until a locked mode was identified from cessation of sawteeth and an $n = 1$ magnetic signature. As shown in figure 4 the data are well fit by $\alpha_B = -1.06 \pm 0.15$ which implies a major-radius scaling $\alpha_R = 0.68 \pm 0.19$ that extrapolates to a threshold $\tilde{B}_{21}/B \approx 0.9 \times 10^{-4}$ in ITER at the density expected in its Ohmic phase (2×10^{19} m^{-3}) prior to the application of auxiliary heating. This is a favourable result in that the original coil control system for ITER was designed to reduce the error field to $\tilde{B}_{err}/B \sim 2 \times 10^{-5}$.

6. Alfvén cascades

The PCI system [25] and the magnetic pick-up coils are being used on Alcator C-MOD to study the physics of Alfvén eigenmodes. Of particular interest are the Alfvén cascades, core-localized modes that exist in reversed-shear plasmas [26, 27]. These modes can be driven by the fast ion population from hydrogen minority ion cyclotron heating and are very sensitive to small changes in the minimum of the q profile resulting in a frequency chirping as the current diffuses. Modelling with the ideal MHD code NOVA-K [28] is being used to model the frequency characteristics of these modes and
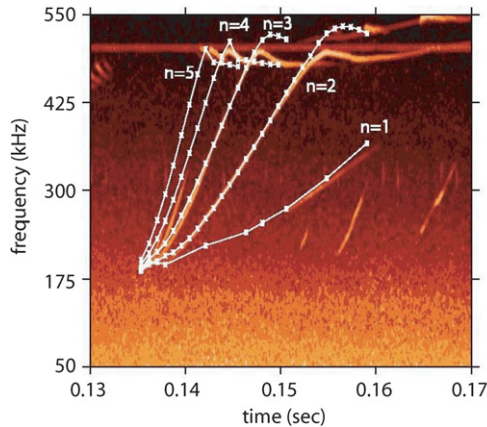
Figure 5. PCI data is shown in red scale, overlaid are numerical results from NOVA in white. The initial frequency calculated from NOVA matches the experimental data within the uncertainty of the experiment.

infer the evolution of the current profile (figure 5). Typical PCI signals from the 32 element detector array show multiply peaked structures for the cascades. Before the development of the 'synthetic' PCI tool used with the NOVA-K results, it was unknown whether this was a measurement of a mode with multiple peaks in its radial structure, or an effect arising from the line integration of density fluctuations. First results from NOVA-K using typical eigenmode solutions with a single peak in the radial structure showed a triplet of peaks in the simulated PCI data, matching closely the experimental data. The application of these methods should allow for more accurate modelling of the central safety factor [29].

7. Turbulence measurements and simulations

Nonlinear gyrokinetic simulations of TEM turbulence in C-MOD have moved beyond comparisons with inferred transport fluxes to a more fundamental comparison with measured density fluctuation spectra. An internal transport barrier ITB that can be generated in C-MOD with off-axis ICRF heating [30], and regulated with on-axis ICRF heating [31, 32], provides vertical localization along viewing chords of the PCI diagnostic, and an opportunity to study particle transport without sources. Previously, we demonstrated that nonlinear gyrokinetic simulations of TEM turbulence provide a quantitative understanding of internal transport barrier control in Alcator C-MOD, with no adjustable model parameters [33]. Recently, a new synthetic diagnostic [34, 35], was added to the GS2 gyrokinetic code to allow direct comparison with chord-integrated density fluctuations measured along the 32 PCI chords. There is excellent agreement between the simulated and measured wavelength spectra over the range $1-8\,\mathrm{cm}^{-1}$ as illustrated in figure 6(b). During on-axis heating of the C-MOD ITB, density fluctuations are strongly increased as TEM modes, a primary candidate to explain electron thermal transport, are driven unstable. The relative increase in density fluctuation level with on-axis heating is reproduced by the GS2 simulations, as shown in figure 6(a).

8. Pedestal physics

The density and pressure attained in the H-mode pedestal remains a key uncertainty in performance projections for ITER and physics-based models are needed for reliable extrapolation from existing tokamaks, despite considerable progress in the development of scaling laws on multiple devices [36]. In order to extrapolate pedestal scalings reliably from existing machines, improvements in physics-based modelling are still needed. Previous studies on C-MOD [37] demonstrated that the H-mode pressure gradient (∇p_e) obeys an I_p^2 scaling with a numerical coefficient that depends on collisionality. Recent work has focused on extending the empirical scaling of pedestal height and widths over a wider parameter range and clarifying our understanding of the roles played by both plasma transport processes and neutral fuelling on pedestal structure [38]. Over the range $I_\mathrm{p} = 0.4-1.5\,\mathrm{MA}$ and $B_\mathrm{T} = 2.7-6.3\,\mathrm{T}$, we observe a nearly linear scaling of edge pedestal density with current with little systematic B_T dependence (figure 7(a)). The robust dependence on a single plasma parameter that is irrelevant to neutral–plasma interactions suggests that the density pedestal is largely defined by plasma transport mechanisms, and not solely by edge particle fuelling. In H-mode plasmas there is typically no gas feed and the density is sustained entirely by wall recycling, and experiment shows a weak dependence of $n_\mathrm{e,ped}$ on line-averaged density prior to the L–H transition. This trend is illustrated in figure 7(b), in which the H-mode pedestal density increases 30–40%, for a factor-of-two variation in n_eL consistent with a previously inferred scaling: $n_\mathrm{e,ped} \propto n_\mathrm{eL}^{0.4}$.

The empirical scaling of the pedestal density width Δ_n differs on C-MOD and DIII-D, with C-MOD observing no dependence of Δ_n on $n_\mathrm{e,ped}$ while DIII-D observes $\Delta_n \propto 1/n_\mathrm{ped}$, the latter being consistent with simple 1D fluid modelling that invokes a radial flux balance between ions and neutrals [39]. A kinetic treatment of neutral transport using the KND code reproduces the fundamental C-MOD trends [38]: as fuelling is increased, the modelled ion density increases weakly while the pedestal width remains roughly constant. Effectively, the increased density causes a greater fraction of the ionization to occur near or outside the foot of the pedestal, leading to a 'self-screening' pedestal. By contrast, at the lower densities prevalent in DIII-D the modelling shows this screening effect to be less substantial, with pedestal width increasing as the fuelling source is reduced in magnitude. On C-MOD, inefficiency of pedestal fuelling is demonstrated experimentally by strong (tens of $\mathrm{T\,1\,s}^{-1}$) gas puffing into an H-mode plasma (figure 7(c) and (d)), whose density pedestal moves outward slightly but does not change in magnitude. Enhanced neutral screening is a consequence of high neutral opacity, which measures the number of ionizations a neutral would be expected to undergo while traversing a distance L. Simple estimates of the opacity in the ITER SOL and pedestal give values far larger than those of most existing tokamaks. However, the opacity of the C-MOD edge can closely approach the ITER value. These results thus suggest an extremely limited capability to control the density pedestal height in ITER through gas fuelling, consistent with the results of ITER modelling efforts [40].
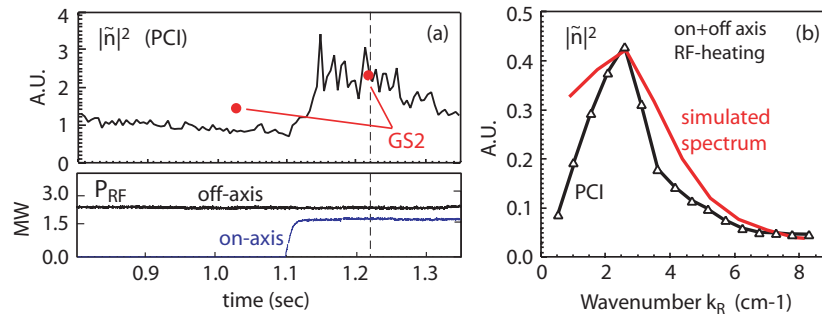
S603

Figure 6. (*a*) Time history of density fluctuation level when on-axis ICRF power is applied to a plasma with an internal transport barrier generated by off-axis ICRF heating. Red points represent the fluctuation level computed by GS2. (*b*) Comparison of measured and simulated k-spectrum at 1.22 s, when RF provided both on- and off-axis heating.
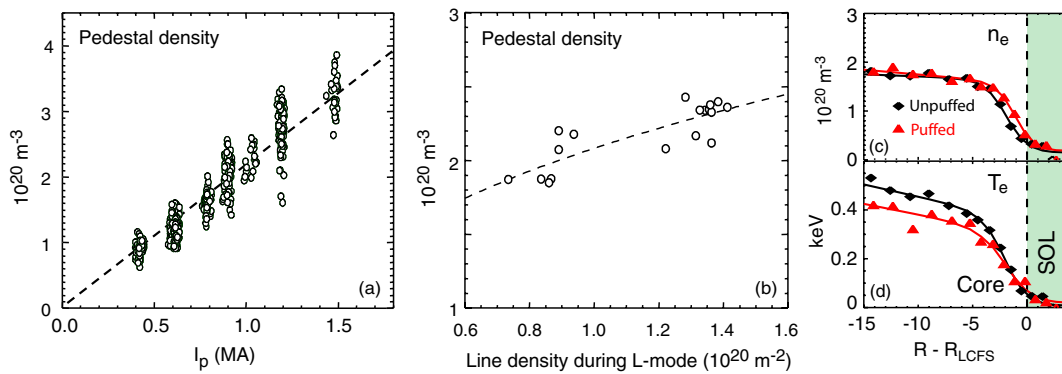

Figure 7. (*a*) Scaling of pedestal density with I_p. (*b*) Scaling of pedestal density with density in preceding L-mode phase. (*c*)–(*d*) Edge Thomson scattering profiles of electron density and temperature in 0.81 MA H-mode plasma before and during strong D_2 puffing (tens of $T 1 s^{-1}$) at the inner wall. The density pedestal shifts radially outward but the height remains essentially unchanged.

9. SOL phase space

Previous analysis [41] of scanning Langmuir–Mach probe data showed that pressure gradients in the SOL of Ohmic L-mode discharges scale as I_p^2 (similar to the scaling of edge pedestal pressure in H-mode plasmas) and that the pressure gradients clamp at similar values of the MHD ballooning parameter $\alpha_{MHD} = q^2 R \beta / L_{pe}$ when the normalized collisionality parameter α_d defined in [41] ($\alpha_d \propto \lambda_e^{1/2} / (q R^{3/4} L_\perp^{1.4})$) is held fixed. Similar trends are observed in ASDEX-Upgrade, which finds that the pressure gradient e-folding length and heat diffusivity in the H-mode edge scales as $L_{nT_e} \sim n / I_p^2$ [42, 43] and that the overall edge behaviour is consistent with a critical-gradient transport paradigm [44]. Over a wide range in machine parameters B_T, I_p and $\bar{n}_e$, the observed SOL states are observed to cluster around a narrow band in the two-dimensional space (α_{MHD}, α_d) as would be expected from electromagnetic fluid drift turbulence (EMFDT). Comparing probe measurements on the low and high-field SOLs revealed that the observed large SOL flows are caused by ballooning-like transport that dumps larger particle fluxes into the low-field region, thereby generating a density imbalance that drives a helical flow in the SOL toward the high-field side.

Recent density scans with $0.1 < n/n_G < 0.5$ over an extended range of I_p and B_T (0.4–1.1 MA, 2.7–5.8 T)

have focused on the effect of the X-point topology on the SOL pressure gradients [45]. As shown in figure 8(*a*), the SOL pressure gradients continue to scale consistently as I_p^2, but with a numerical value that depends on the X-point topology, with higher gradients attained in the LSN configuration. For a given X-point configuration, data from different plasma currents collapse into a narrow band when plotted in EMFDT phase space (confirming the dominant I_p^2 scaling), but the LSN and USN datasets form two separate bands, with lower null achieving higher values of α_{MHD} (figure 8(*b*)). As illustrated in figure 8(*c*), the SOL plasma flows are dramatically different in the LSN versus USN configurations, and the range of collisionality parameter α_d where the LSN obtains higher α_{MHD} corresponds to the region where there is a significant difference in the parallel Mach number on the low-field side. This indicates that co-current flows in the SOL are associated with higher pressure gradients, and suggests that flow is another controlling variable in the EMFDT phase space ($\alpha_{MHD}, \alpha_D, M$). Recent experiments with reversed B_T and I_p in USN plasmas confirm these results.

10. Imaging of turbulence with gas puffs

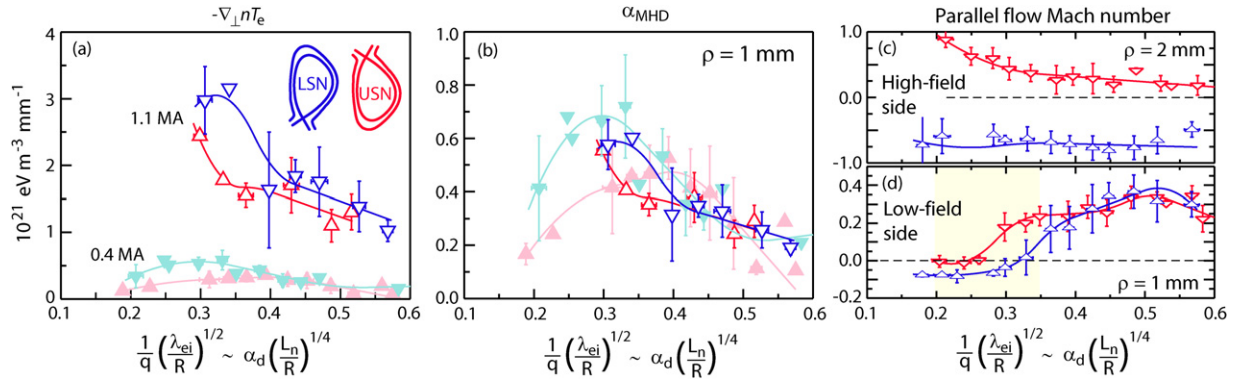Electrostatic turbulence in the SOL of C-MOD has been measured [46] using 1D and 2D gas puff imaging (GPI)

Figure 8. (*a*) Electron pressure gradients in the plasme edge as a function of a local, inverse collisionality parameter [41]. The pressure gradient scales dominantly with I_p^2 resulting in (*b*) similar values of α_{MHD} when the local collisionality is the same. (*c*) Near-sonic parallel flows on the high-field side change direction in going from LSN to USN. (*d*) Parallel flows on the low-field side tend to be less co- current directed in USN over the collisionality range where α_{MHD} is also lower. Flow data are averaged over $I_p = 0.4$, 0.8 and 1.1 MA.
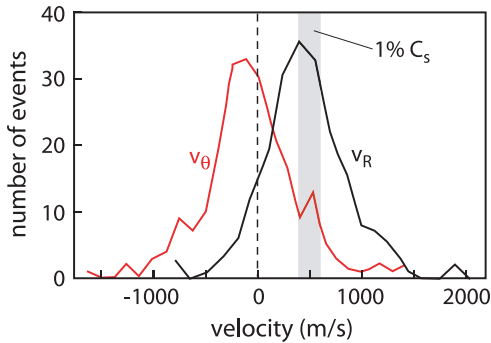

Figure 9. Frequency distribution of velocity for large-amplitude fluctuation structures inferred from fast camera imaging of gas puffs. The shaded area represents 1% C_s in the mid-to-far-SOL ($\rho = 10$–20 mm).

and Langmuir probes. The cross-correlation between light fluctuations seen by the 1D GPI (δI) and the density (δn) and ($\delta\phi$) potential fluctuations seen in the Langmuir probe was measured by aligning the two diagnostics with a parallel separation of 3 m along the same magnetic field line in the SOL. The cross-correlation between (δI, δn) was maximum when the two diagnostics were on the same field line, but the cross-correlation between (δI, $\delta\phi$) showed a poloidal dipole structure centred on the field line, in qualitative agreement with the blob model for edge turbulence structures [47, 48]. The radial and poloidal velocity distribution of the blob structures in the SOL was directly measured using the 2D GPI imaging system, as shown in figure 9. Qualitatively, the blob structures observed in C-MOD are similar to the 'filament' structures observed in the edge of MAST [49]. Ninety per cent of the structures are observed to propagate radially outward with a most probable speed of $\sim$500 m s^{-1}, or about 1% of the local ion sound speed. The magnitude of this speed is roughly comparable to that predicted by models of blob propagation in the SOL.

11. ELMs

The standard H-mode regime in C-MOD is enhanced D_α [50] in which a quasi-coherent mode localized in the pedestal
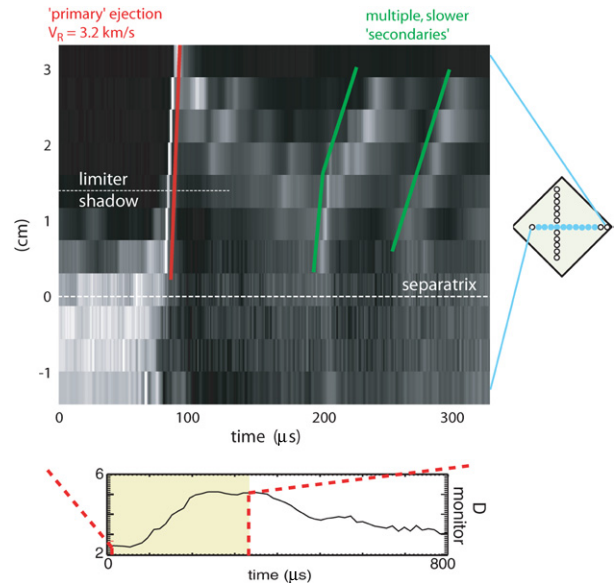

Figure 10. Structure of primary and secondary ejections during discrete ELMs as measured by a radial array of views at the plasma edge on the low-field side. The diamond illustrates the location of vertical and radial diode arrays at the outboard plasma edge.

region increases particle transport and thereby avoids excessive impurity and pressure build-up that trigger discrete ELMs or radiative collapse. Recently, a new region of H-mode operational space at low collisionality ($\nu^{ped} < 1$) and high triangularity ($\delta > 0.75$) has been accessed where discrete, relatively large ELMs are present [51] similar to previous observations in DIII-D [52]. These ELMs do not destroy the temperature or density pedestal, and the energy loss per ELM is typically 10–20% of W_{ped}. Their structure and evolution have been studied using magnetics and D_α emission from GPI. The emissions from outboard vertical and radial arrays of views and from an inboard radial array are analyzed. A complex time history is observed, with a 200–400 kHz, $n_{toroidal} \sim 10$ precursor oscillation starting inside the separatrix, followed by the ejection of rapidly propagating ($v_R = 0.5$–8.0 km s^{-1}) primary filaments (figure 10). The primary ejection into

the outboard SOL is coincident with the onset of a short-lived 0.5–1 MHz magnetic oscillation. This initial evolution is followed by multiple slower secondary filament ejections.

12. Facility upgrades and future plans

Over the next two years, a number of facility upgrades on C-MOD will enhance its capability to study AT plasma regimes and ITER-relevant physics and engineering issues. A toroidal cryopump is now being installed on the inboard side of the upper divertor chamber to provide active density control needed to reduce the density to values consistent with efficient LHCD. Initial test-stand performance has demonstrated pumping speeds of $10^4 \, \mathrm{l} \, \mathrm{s}^{-1}$ for deuterium gas, which is sufficient to deplete the C-MOD particle inventory several times per plasma discharge. A second lower hybrid launcher will be installed to increase the power capability to 4 MW (source power), and a new 4-strap RF antenna will replace two of the existing 2-strap antennas with no net change to the total RF power capability. The ICRF system will be upgraded with fast ferrite tuners to allow one antenna to tune through changes in plasma configuration and ELMs on a 1 ms time scale. Based on the promising results of tungsten brush tiles in the lower divertor this run campaign (no evidence of significant tungsten emission), a complete toroidal ring of tungsten tile modules will be installed in the lower divertor based on an improved 'lamallae' design. The long-pulse diagnostic neutral beam is being rotated from its current orientation (exactly perpendicular to the toroidal field) $7°$ in the toroidal direction to eliminate a population of ripple-trapped fast ions that confuses the calibration of the MSE diagnostic. A number of extensive diagnostic upgrades are also in progress, including an imaging x-ray crystal spectrometer for fine-scale profile measurements ($\sim$40 spatial chords) of T_i and v_ϕ, PCI upgrades to extend its measurement capability to $k \sim 60 \, \mathrm{cm}^{-1}$, a swept-frequency reflectometer to measure the density fluctuation correlation length at $2 \times 10^{20} \, \mathrm{m}^{-3}$, a second fast-framing GPI camera to view the lower divertor, a 20-channel polarimeter to supplement the MSE q-profile measurements, and installation of 'marker' tiles to improve our understanding of the localization of impurity sources.

Acknowledgments

References

[1] Dux R. *et al* 2006 *Proc. 21st Int. Conf. on Fusion Energy 2006 (Chengdu)* (Vienna: IAEA) CD-ROM file EX/3-3Ra and http://www-naweb.iaea.org/napc/physics/FEC/FEC2006/html/index.htm

[2] Lipschultz B. *et al* 2006 *Phys. Plasmas* **13** 056117
[3] Perkins F.W. 1989 *Nucl. Fusion* **29** 583
[4] D'Ippolito D.A., Myra J.R., Bureš M. and Jacquinot J. 1991 *Plasma Phys. Control. Fusion* **33** 607
[5] Wukitch S. *et al* 2007 *J. Nucl. Mater.* **363–365** 491–7
[6] Nieuwenhove R Van and Oost R Van 1989 *J. Nucl. Mater.* **162–164** 288
[7] Colas L *et al* RF-sheath physics assessment of tore supra ICRF antenna designs *14th Topical Conf. on Radio Frequency Power in Plasmas (Oxnard, CA)* ed T.K. Mau and J. deGrassie p 134
[8] D'ippoltio D.A. *et al* 1998 *Nucl. Fusion* **38** 10 1543
[9] Bureš M. *et al* 1991 *Plasma Phys. Control. Fusion* **33** 937
[10] Causey R. *et al* 1999 *J. Nucl. Mater.* **266–269** 467
[11] Mueller D. *et al* 1997 Tritium retention and removal on TFTR *17th IEEE/NPSS Symp. on Fusion Engineeering 1997 (San Diego, CA, USA)* vol 1 p 279–82
[12] Andrew P. *et al* 1999 *J. Nucl. Mater.* **266–269** 153–9
[13] Tanabe T. *et al* 2005 *J. Nucl. Mater.* **345** 89
[14] Wright G.M. *et al* 2007 *J. Nucl. Mater.* **363–365** 977–83
[15] Brambilla M. 1976 *Nucl. Fusion* **16** 47
[16] Liptac J.E. 2006 Lower hybrid modelling and experiments on Alcator C-MOD *Doctoral Thesis* Department of Nuclear Science and Engineering, MIT
[17] Harvey R.W. and McCoy M.G. 1993 *Proc. IAEA Technical Committee Meeting on Advances in Simulation and Modelling of Thermonuclear Plasmas (Montreal, 1992)* (Vienna: IAEA) pp 489–526
[18] Giruzzi G. *et al* 1997 *Nucl. Fusion* **37** 673
[19] Whyte D.G. *et al* 2002 *Phys. Rev. Lett.* **89** 055001
[20] Granetz R. *et al* 2006 *Proc. 21st Int. Conf. on Fusion Energy 2006 (Chengdu)* (Vienna: IAEA) CD-ROM file EX/4-3 and http://www-naweb.iaea.org/napc/physics/FEC/FEC2006/html/index.htm
[21] Izzo V. *et al* 2006 *Proc. 21st Int. Conf. on Fusion Energy 2006 (Chengdu)* (Vienna: IAEA) CD-ROM file TH/P3-15 and http://www-naweb.iaea.org/napc/physics/FEC/FEC2006/html/index.htm
[22] Connor J and Taylor B 1997 *Nucl. Fusion* **17** 1047
[23] Wolfe S.M. *et al* 2005 *Phys. Plasmas* **12** 56110-1-10
[24] Buttery R.J. *et al* 1999 *Nucl. Fusion* **39** 1827
[25] Porkolab M. *et al* 2006 *IEEE Trans. Plasma Sci.* **34** 229–334
[26] Sharapov S. *et al* 2001 *Phys. Lett.* A **289** 127
[27] Takechi M. *et al* 2005 *Phys. Plasmas* **12** 082509
[28] Cheng C.Z. and Chance M.S. 1987 *J. Comput. Phys.* **71** 124
[29] Porkolab M. *et al* 2006 *Proc. 21st Int. Conf. on Fusion Energy 2006 (Chengdu)* (Vienna: IAEA) CD-ROM file EX/P6-16 and http://www-naweb.iaea.org/napc/physics/FEC/FEC2006/html/index.htm
[30] Rice J.E. *et al* 2001 *Nucl. Fusion* **41** 277
[31] Wukitch S.J. *et al* 2002 *Phys. Plasmas* **9** 2149
[32] Rice J.E. *et al* 2002 *Nucl. Fusion* **42** 510
[33] Ernst D.R. *et al* 2004 *Phys. Plasmas* **11** 2637
[34] Ernst *et al* 2006 *Proc. 21st Int. Conf. on Fusion Energy 2006 (Chengdu)* (Vienna: IAEA) CD-ROM file TH/1-3 and http://www-naweb.iaea.org/napc/physics/FEC/FEC2006/html/index.htm
[35] Long A and Ernst D.R. 2005 *Bull. Am. Phys. Soc.* **50** GP1.48 153
[36] Cordey J.G. 2003 *Nucl. Fusion* **43** 670
[37] Hughes J.W. *et al* 2002 *Phys. Plasmas* **9** 3019
[38] Hughes J.W. *et al* 2006 *Phys. Plasmas* **13** 056103
[39] Groebner M.A. *et al* 2004 *Nucl. Fusion* **44** 204
[40] Kukushkin A.S. *et al* 2003 *Nucl. Fusion* **43** 716
[41] Labombard B. *et al* 2005 *Nucl. Fusion* **45** 1658
[42] McCormick K. *et al* 1999 *J. Nucl. Mater.* **266–269** 99
[43] Kim J.W. *et al* 2001 *J. Nucl. Mater.* **290–293** 644
[44] Neuhauser J. *et al* 2002 *Plasma Phys. Control. Fusion* **44** 855
[45] Labombard B. *et al* 2007 *J. Nucl. Mater.* **363–365** 517–21

[46] Grulke O., Terry J.L., Labombard B. and Zweben S.J. 2006 *Phys. Plasmas* **13** 102306
[47] Myra J.R. and Dippolto D. 2005 *Phys. Plasmas* **12** 092511
[48] Garcia O.E. *et al* 2005 *Phys. Plasmas* **12** 090701
[49] Kirk A. *et al* 2006 *Plasma Phys. Control. Fusion* **48** B433
[50] Greenwald M. *et al* 1999 *Phys. Plasmas* **6** 1943
[51] Terry J.L. *et al* 2007 Investigation of ELMs in Alcator C-MOD, *17th PSI Conf. (Hefei, China) J. Nucl. Mater.* submitted
[52] Leonard A.W. *et al* 2003 *Phys. Plasmas* **10** 1765